INTERNATIONAL JOURNAL FOR NUMERICAL METHODS IN FLUIDS
Int. J. Numer. Meth. Fluids **28**: 983–1007 (1998)

SIMULATIONS OF 2D AND 3D THERMOCAPILLARY FLOWS BY A LEAST-SQUARES FINITE ELEMENT METHOD

LI Q. TANG[1], JAMIE L. WRIGHT[2] AND TATE T.H. TSANG*
Department of Chemical and Materials Engineering, University of Kentucky, Lexington, KY 40506-0046, USA

SUMMARY

Numerical results for time-dependent 2D and 3D thermocapillary flows are presented in this work. The numerical algorithm is based on the Crank–Nicolson scheme for time integration, Newton's method for linearization, and a least-squares finite element method, together with a matrix-free Jacobi conjugate gradient technique. The main objective in this work is to demonstrate how the least-squares finite element method, together with an iterative procedure, deals with the capillary-traction boundary conditions at the free surface, which involves the coupling of velocity and temperature gradients. Mesh refinement studies were also carried out to validate the numerical results.

1. INTRODUCTION

Fluid motion is mainly driven by pressure force, shear stresses, buoyancy force and surface tension forces. Recently, buoyancy- and surface tension-driven flows, i.e. thermocapillary flows, became increasingly important in the understanding of welding and crystal growth processes. In thermocapillary flows, thermal gradients along a free surface induce surface tension gradients, which result in a net surface tension force acting on the free surface.

The behavior of thermocapillary flows is characterized by a dimensionless number, the Marangoni number, *Ma* (Peclet number for thermocapillary flows). Another outstanding characteristic of thermocapillary flows is that velocity and temperature gradients are interrelated on the free surface as boundary conditions. Thus, a robust numerical method is required to deal with such coupling of velocity and temperature gradients on the free surface.

Zebib *et al.* [1] present a finite difference method for steady state two-dimensional thermocapillary flows. Carpenter and Homsy [2] used a similar finite difference method with a streamfunction and vorticity formulation. Shyy and Chen [3] present steady state, two-dimensional results for low Prandtl number fluids in solidification processes. It is well known that the oscillatory behavior of low Prandtl number melts has significant effects on the quality of crystals, semiconductor materials and alloys. Thus, much effort has been devoted to the study of oscillatory thermocapillary flows. Hadid and Roux [4] and Mundrane and Zebib [5]

---

* Correspondence to: Department of Chemical and Materials Engineering, University of Kentucky, Lexington, KY 40506-0046, USA.

[1] Current address: Enterprise Management System Group, The Prudential Insurance Company of America, Roseland, NJ 07068.

[2] Current address: Dow Corning Corporation, PO Box 310, Carrollton, KY 41008.

CCC 0271–2091/98/160983–25$17.50

Received 13 May 1996
Revised 3 November 1997

investigated oscillatory states in two-dimensional thermocapillary flows for low Prandtl number fluids. Kanoff and Grief [6] showed oscillatory thermocapillary flows for a fluid with a quadratic dependence of surface tension on temperature.

Numerical results for three-dimensional thermocapillary flows are relatively scarce in the literature. Mundrane and Zebib [7] present results for thermocapillary flows in a rectangular box. Using a finite difference technique with a primitive variable approach on a non-staggered grid, Babu and Korpela [8] provide results of thermocapillary flows in a cubic box for Reynolds numbers of 100 and 300, with Prandtl numbers of 0.01 and 1.0.

In this work, a least-squares finite element method (LSFEM) is used to simulate thermocapillary flows. The main advantage of the LSFEM is that it leads to symmetric, positive definite (SPD) linear systems that can be solved efficiently by a matrix-free preconditioned conjugate gradient method, with minimum computer memory requirement for three-dimensional flows and transport processes. Recently, it has been proven that the LSFEM is a promising method for fluid flows and transport processes with Dirichlet boundary conditions [9–15]. Theoretical results using the LSFEM for a variety of differential equations have also been obtained [16–19]. The objective in this work is to demonstrate how the LSFEM deals with the capillary-traction boundary conditions at the free surface, which involves the coupling of velocity and temperature gradients.

2. MATHEMATICAL MODELING

2.1. Well-posed problem

Consider time-dependent incompressible fluid flows in a domain $\Omega \subset \mathbb{R}^3$ bounded by $\Gamma_D \cup \Gamma_N$, where Γ_D and Γ_N are the Dirichlet and capillary-traction boundaries, respectively, and $\Gamma_D \cap \Gamma_N = 0$. Figure 1 shows the geometry of a cubic cavity. The left wall ($z = 0$) is heated at high temperature T_h and the right wall ($x = 1$) is cooled at low temperature T_c. The other walls are adiabatic, except the top surface which is free and in contact with the air above. The fluid motions are induced by surface tension gradients on the liquid–gas interface, where

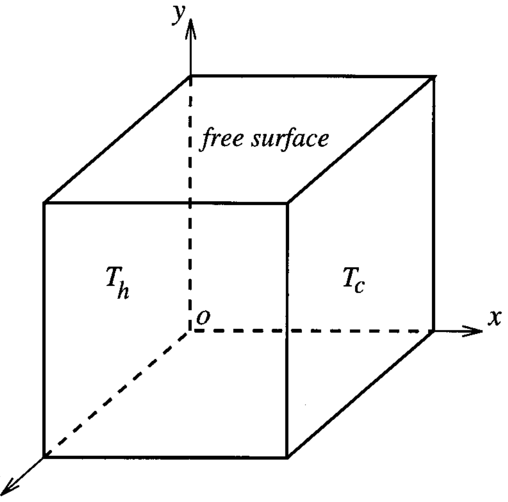

Figure 1. Flow configuration of three-dimensional thermocapillary flows.

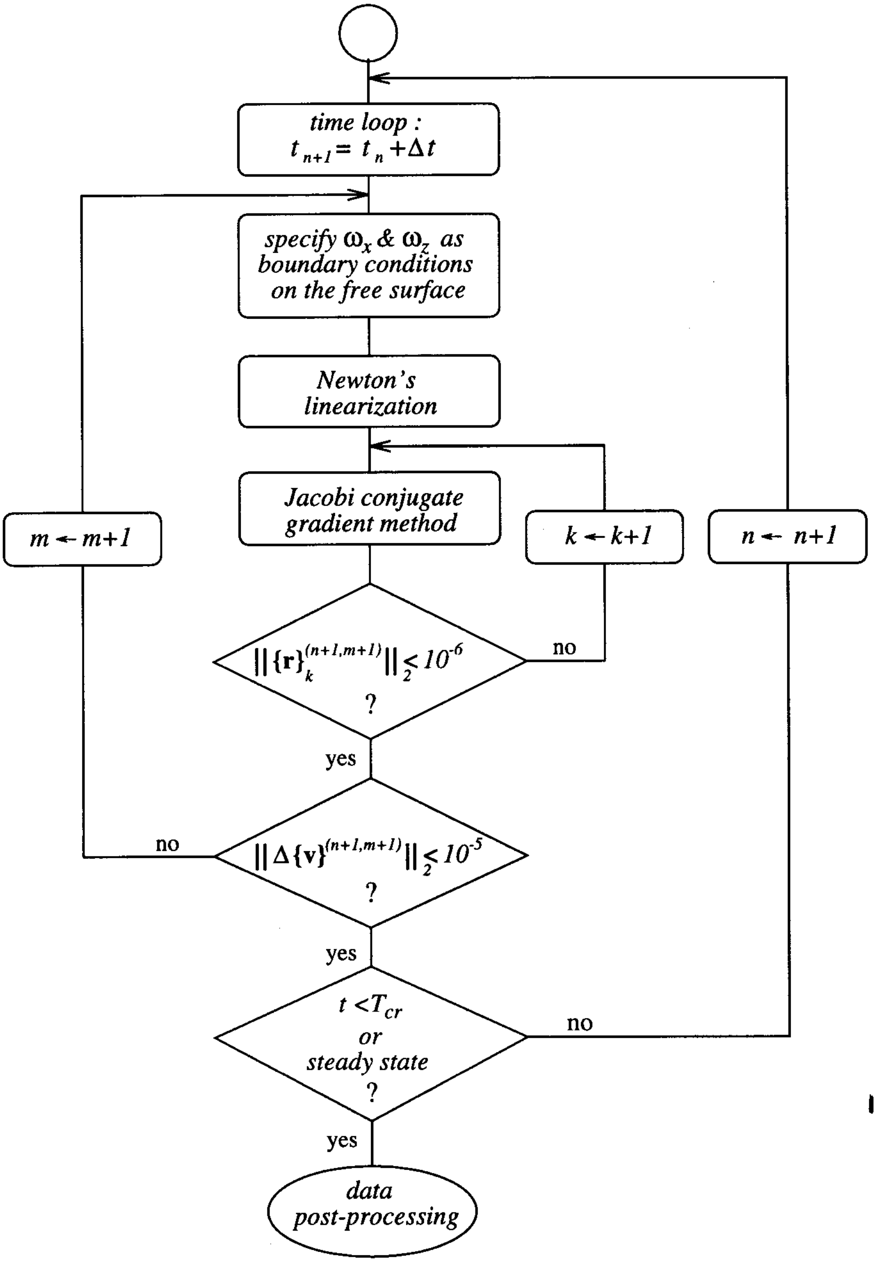

Figure 2. Basic structure of the algorithm of time-dependent LSFEM with JCG.

temperature gradients exist. The effect of the surface deformation is neglected for the condition of small capillary number $Ca = \gamma T_r/\sigma_r$. The mass, momentum and energy conservation are described by the Navier–Stokes equations and energy balance equation with the Boussinesq assumption. The spatial and temporal co-ordinates are denoted by $\mathbf{x} = \{x, y, z\}^T \in \Omega$ and $t \in (0, \infty)$. The governing equations in dimensionless form are as follows, in $\Omega \times (0, \infty)$

$$\frac{\partial \mathbf{u}}{\partial t} + \mathbf{u}\cdot\nabla\mathbf{u} + \nabla p - \frac{1}{Re}\nabla^2\mathbf{u} - \frac{Bo}{Re}\,T\frac{\mathbf{g}}{|\mathbf{g}|} = 0, \tag{1}$$

$$\nabla\cdot\mathbf{u} = 0, \tag{2}$$

$$\frac{\partial T}{\partial t} + \mathbf{u}\cdot\nabla T - \frac{1}{Ma}\nabla^2 T = 0, \tag{3}$$

where $\mathbf{u} = \{u, v, w\}^T$ is the velocity vector, p is the pressure deviation from hydrostatic, and T the temperature; $Re = \gamma T_r H/\mu v$ is the Reynolds number, $Pr = v/\alpha$ is the Prandtl number, $Ma = Re\cdot Pr$ is the Marangoni number, $Bo = Gr/Re$ is the Bond number, and $Gr = |\mathbf{g}|\beta T_r H^3/v^2$ is the Grashof number; $\gamma = -\partial\sigma/\partial T|_{(T=T_r)}$ is the surface tension temperature coefficient, $\sigma = \sigma_r - \gamma(T - T_r)$ is the surface tension, T_r is the reference temperature, H is the characteristic length, μ is the fluid viscosity, ρ is the fluid density, $v = \mu/\rho$, α is the thermal diffusivity, $\mathbf{g}$ is the gravity acceleration, and β is the thermal expansion coefficient of the fluid.

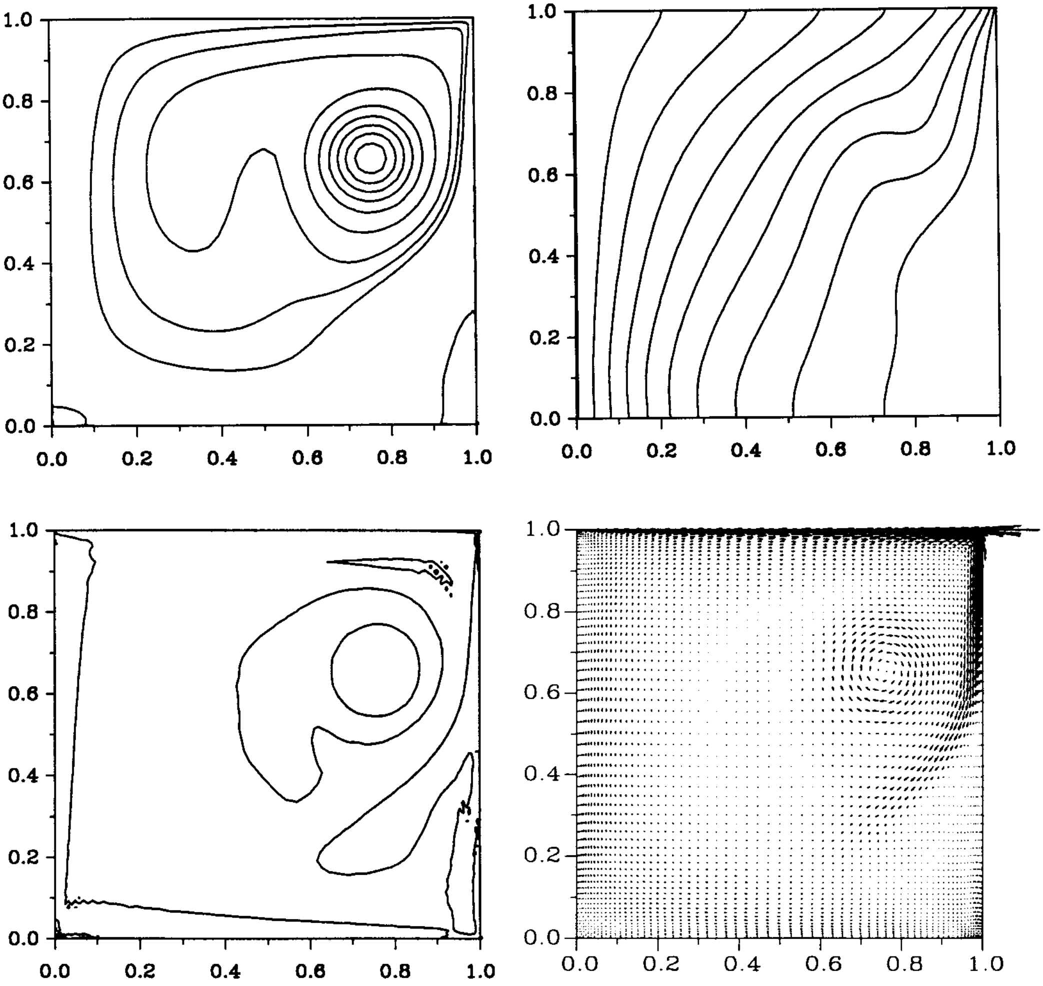

Figure 3. Augmenting flow for $Ma = 8.4 \times 10^3$, $Pr = 0.0149$ and $Gr = 3.09 \times 10^6$ at steady state: (a) streamfunction, (b) temperature contours, (c) vorticity contours and (d) velocity vectors.

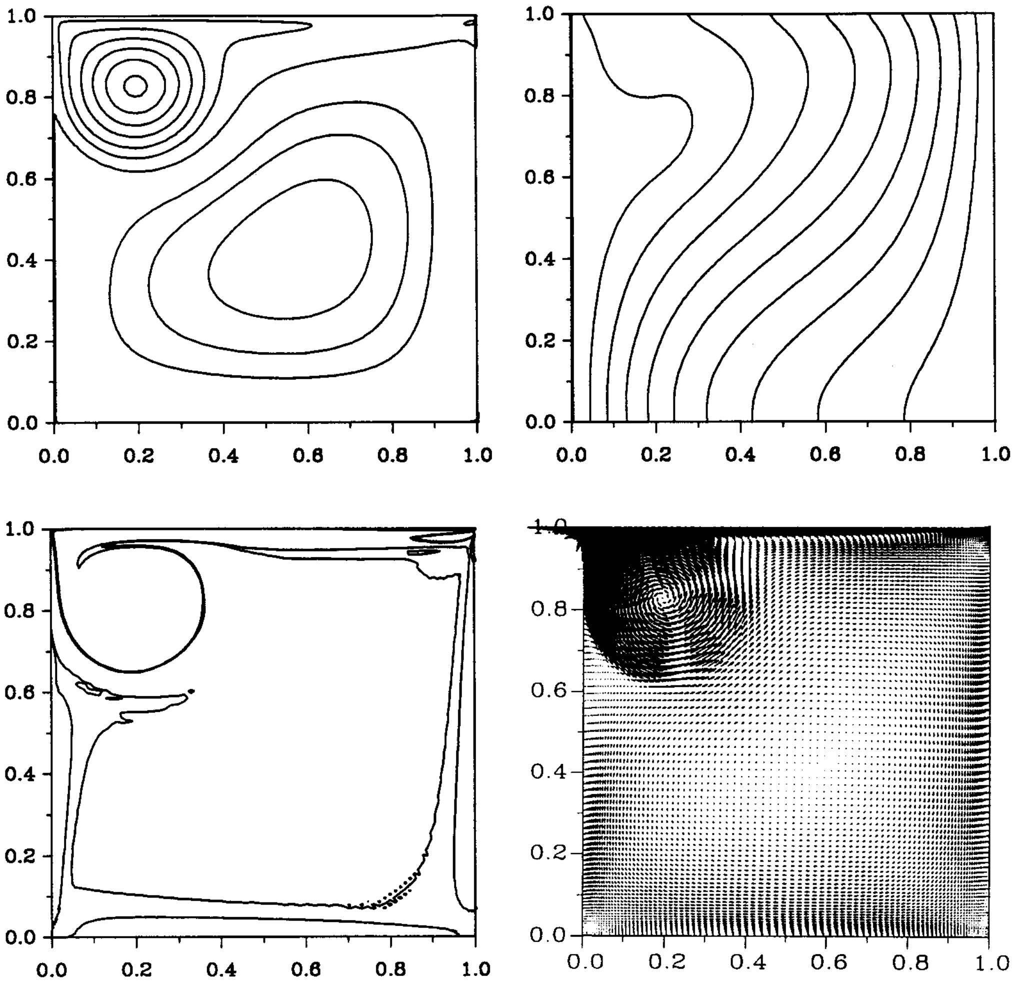

Figure 4. Opposing flow for $Ma = 8.4 \times 10^3$, $Pr = 0.0149$ and $Gr = 3.09 \times 10^6$ at steady state: (a) streamfunction, (b) temperature contours, (c) vorticity contours and (d) velocity vectors.

In this work, the surface deformation is neglected. This assumption is justified in the case of small capillary number [1]. It also simplifies numerical simulations.

Initially, it is assumed that the fluid remains motionless, heat conduction is dominant and temperature distribution is linear along the x-direction,

$$\left.\begin{aligned} \mathbf{u} &= 0 \\ T &= \frac{1}{2} - x \end{aligned}\right\}, \quad \text{for } t = 0. \tag{4}$$

The boundary conditions, in dimensionless form, for adiabatic or isothermal walls and the free surface are as follows, for $t \geq 0$,

$$u = v = w = 0, \quad \text{on } x, z = 0, 1, \tag{5}$$

$$u = v = w = 0, \quad \text{on } y = 0, \tag{6}$$

$$v = 0, \quad \text{on } y = 1, \tag{7}$$

$$T = \frac{1}{2}, \quad \text{on } x = 0, \tag{8}$$

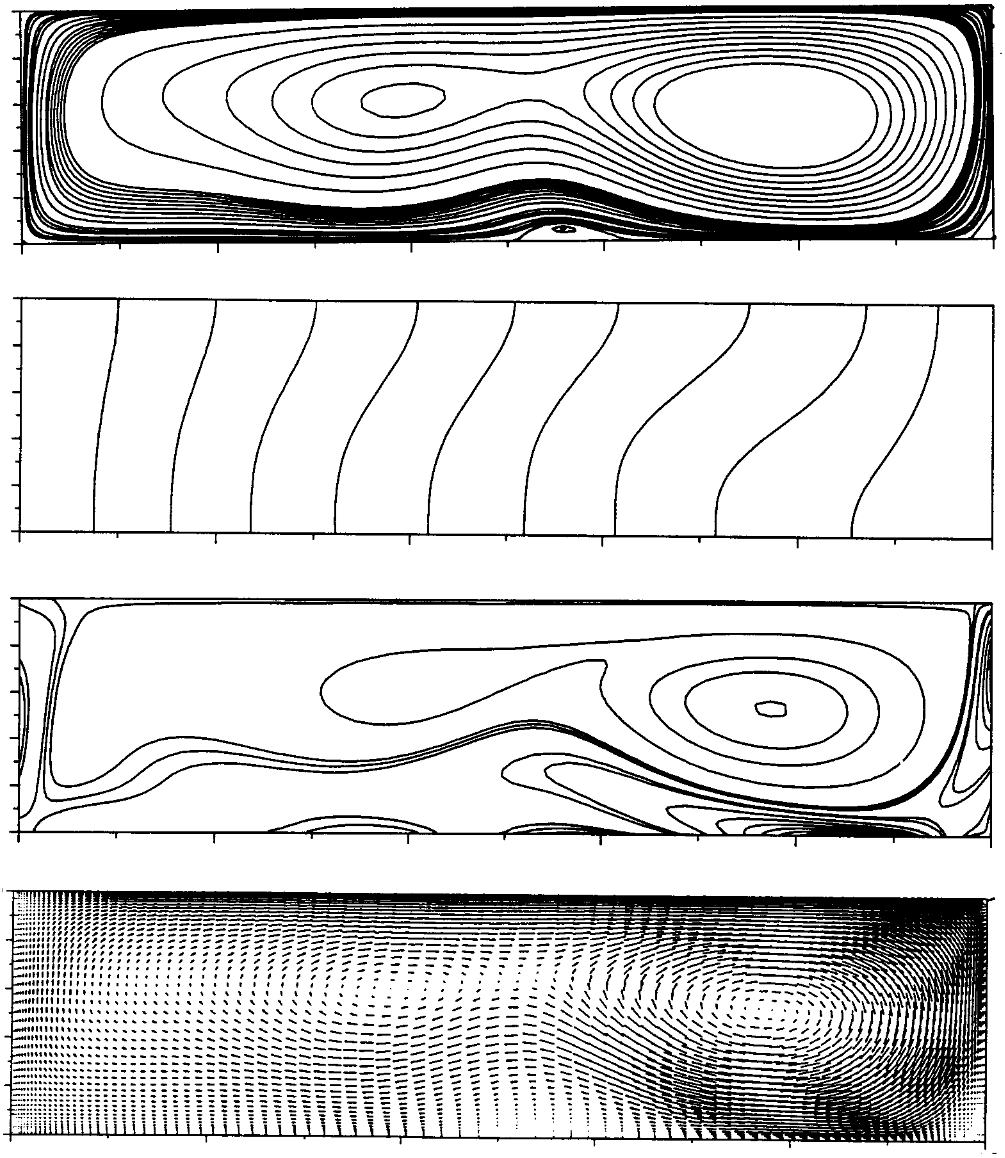

Figure 5. Results for $Re = 67$, $Pr = 0.0149$ and $Gr = 2.0 \times 10^4$ at the dimensionless time level of 45 in the periodic state regime: (a) streamfunction, (b) temperature contours (c) vorticity contours and (d) velocity vectors.

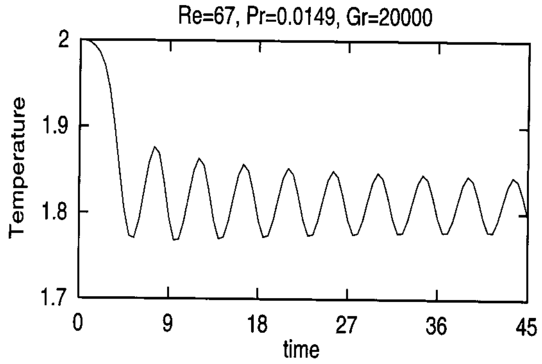

Figure 6. Time history of dimensionless temperature at the center of the cavity.

$$T = -\frac{1}{2}, \quad \text{on } x = 1, \tag{9}$$

$$\frac{\partial T}{\partial z} = 0, \quad \text{on } z = 0, 1, \tag{10}$$

$$\frac{\partial T}{\partial y} = 0, \quad \text{on } y = 0, 1, \tag{11}$$

$$\frac{\partial u}{\partial y} = -\frac{\partial T}{\partial x}, \quad \frac{\partial w}{\partial y} = -\frac{\partial T}{\partial z}, \quad \text{on } y = 1. \tag{12}$$

The thermocapillary flow problem involves three types of boundary conditions: the Dirichlet-type boundary conditions (5)–(9), the Neumann-type boundary conditions (10) and (11) and the capillary-traction boundary conditions (12). On the free surface, both velocity and temperature gradients are unknown and need to be determined.

There are three constraints for the incompressible flow:
Constraint 1. The boundary value $\mathbf{u}_d$ satisfies

$$\int_{\Gamma_\mathrm{D}} \mathbf{n}\cdot\mathbf{u}_d \,\mathrm{d}S = 0, \quad \text{for } t \geq 0. \tag{13}$$

Constraint 2. The initial velocity $\mathbf{u}_0 = \{u_0, v_0, w_0\}^T$ is subject to

$$\nabla\cdot\mathbf{u}_0 = 0, \quad \text{in } \Omega. \tag{14}$$

Constraint 3. The initial velocity $\mathbf{u}_0$ and the boundary value $\mathbf{u}_d$ are subject to

$$\mathbf{n}\cdot\mathbf{u}_0 = \mathbf{n}\cdot\mathbf{u}_d, \quad \text{on } \Gamma_\mathrm{D}. \tag{15}$$

By Equation (15), Constraint 1 also requires the initial velocity profile to satisfy

$$\int_{\Gamma_\mathrm{D}} \mathbf{n}\cdot\mathbf{u}_0 \,\mathrm{d}S = 0, \quad \text{for } t = 0, \tag{16}$$

where **n** is the normal vector. In summary, Constraint 1 requires that the mass conservation law must be satisfied at any time and Constraint 2 demands that fluid flow must be divergence-free in the domain Ω initially. If any of the three constraints are violated, the Navier–Stokes problem is ill-posed and has no solution [20,21].

2.2. *First-order formulation*

Introducing vorticity, $\boldsymbol{\omega} = \{\omega_x, \omega_y, \omega_z\}^T$ and heat flux $\mathbf{q} = \{q_x, q_y, q_z\}^T$, the initial boundary value problem is reduced into the first-order formulation as

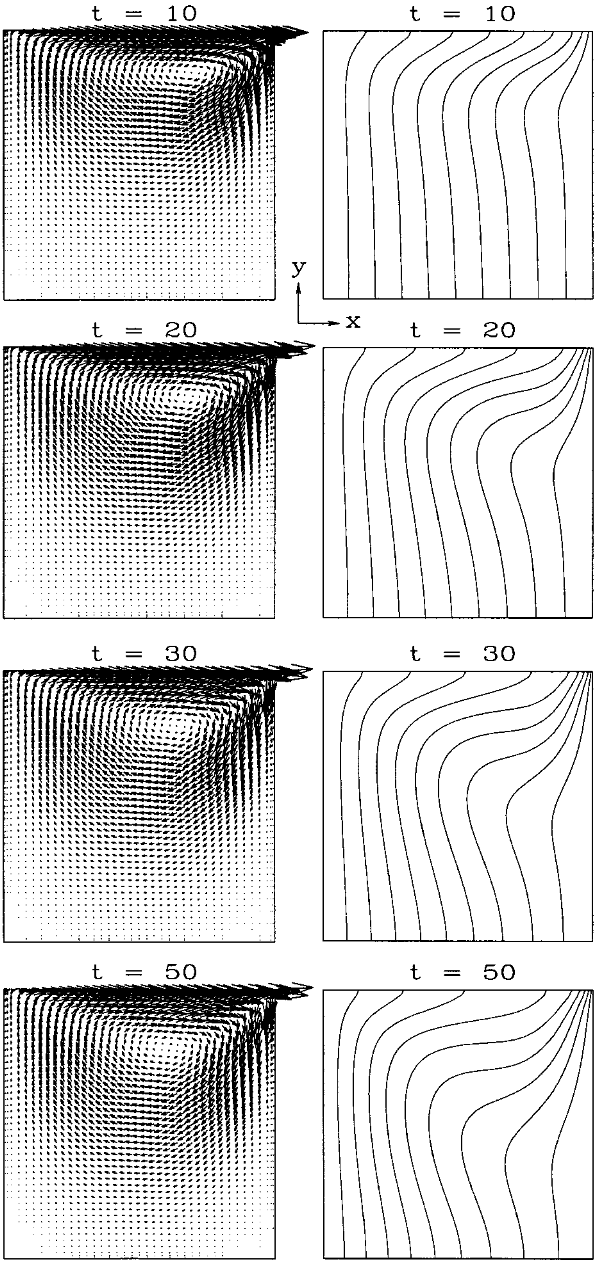

Figure 7. Transient velocity vectors and temperature contours on the plane of $z = 0.5$ for $Re = 1000$, $Pr = 1.0$ ($Ma = 1000$).

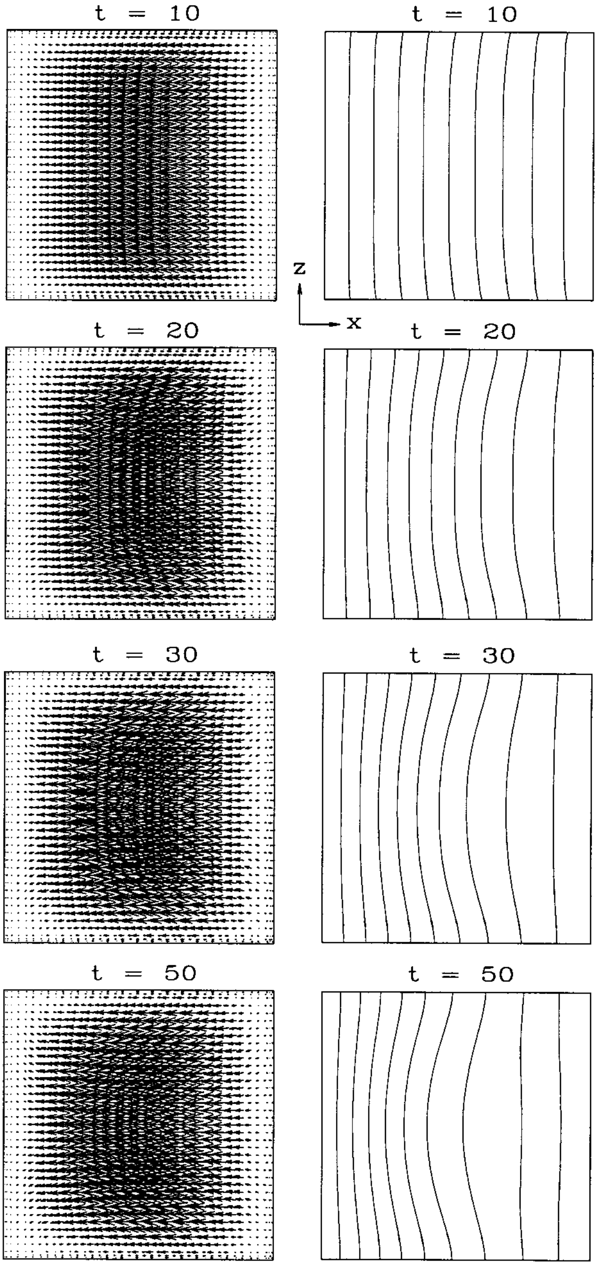

Figure 8. Transient velocity vectors and temperature contours on the plane of $y = 0.5$ for $Re = 1000$, $Pr = 1.0$ ($Ma = 1000$).

$$\frac{\partial \mathbf{u}}{\partial t} + \mathbf{u} \cdot \nabla \mathbf{u} + \nabla p + \frac{1}{Re} \nabla \times \boldsymbol{\omega} - \frac{Bo}{Re} T \frac{\mathbf{g}}{|\mathbf{g}|} = 0, \tag{17}$$

$$\nabla \cdot \mathbf{u} = 0, \tag{18}$$

$$\boldsymbol{\omega} - \nabla \times \mathbf{u} = 0, \tag{19}$$

$$\frac{\partial T}{\partial t} + \mathbf{u} \cdot \nabla T + \nabla \cdot \mathbf{q} = 0, \tag{20}$$

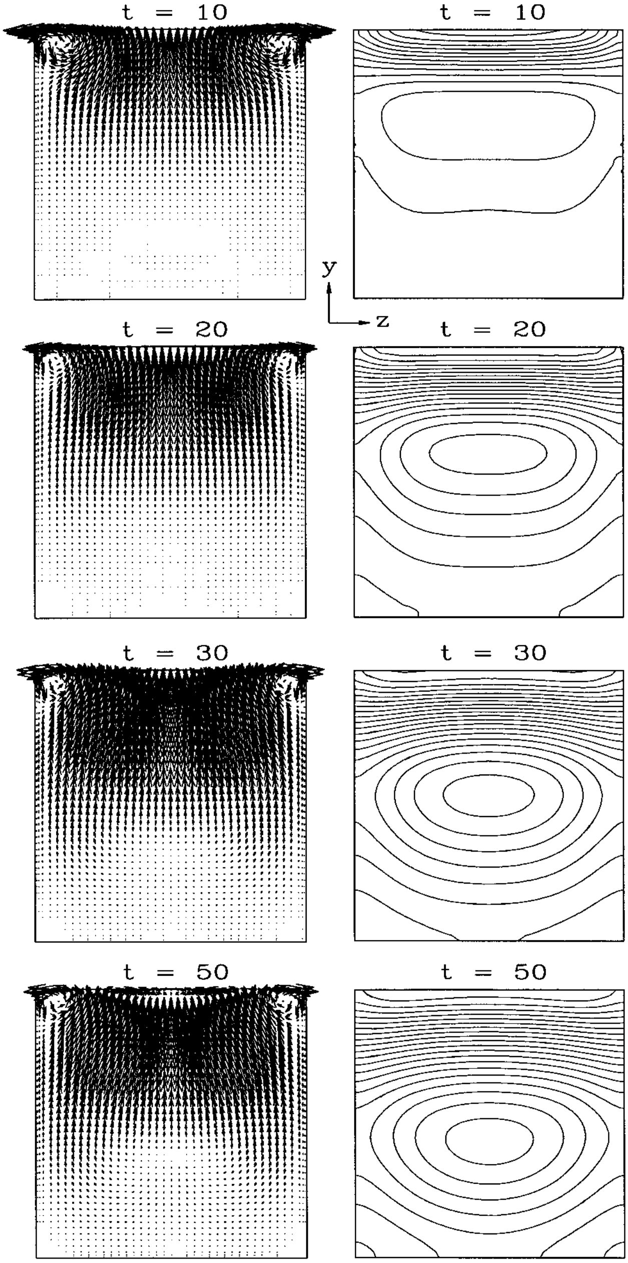

Figure 9. Transient velocity vectors and temperature contours on the plane of $x = 0.5$ for $Re = 1000$, $Pr = 1.0$ ($Ma = 1000$).

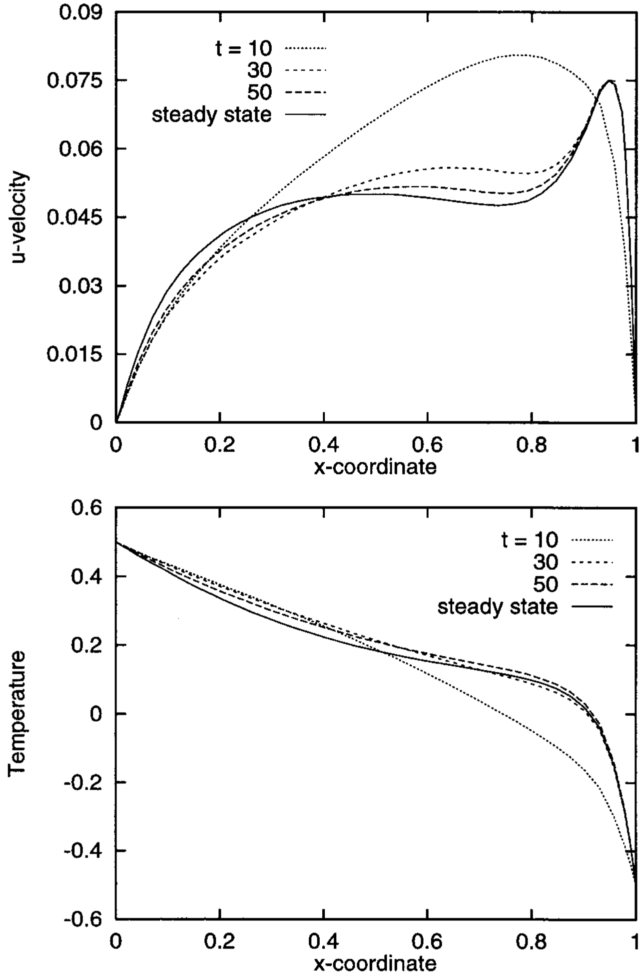

Figure 10. Distributions of velocity u and temperature T along $z = 0.5$ on the free surface at different time levels for $Re = 1000$, $Pr = 1.0$ ($Ma = 1000$).

$$\mathbf{q} + \frac{1}{Ma} \nabla T = 0. \tag{21}$$

Since vorticity ω and heat flux $\mathbf{q}$ are involved in the first-order system of equations, two additional constraints are needed to restrict the first-order elliptic system (17)–(21),
Constraint 4. The solenoidality of vorticity:

$$\nabla \cdot \omega = 0. \tag{22}$$

Constraint 5. The non-rotationality of heat flux:

$$\nabla \times \mathbf{q} = 0. \tag{23}$$

The properties of these constraints have been discussed in detail by Jiang and Povinelli [11], Tang [22] and Tang and Tsang [12,15].

From Equations (4) and (21), an additional initial condition should be specified,

$$q_x = \frac{1}{Ma}, \quad \text{at } t = 0, \tag{24}$$

as consistent with the assumption of the linear temperature distribution (4). Since the equation system (17)–(23) is first-order, only Dirichlet-type boundary conditions are required for well-posedness. The boundary conditions for temperature gradients on the vertical walls (10) and (11) and for velocity and temperature gradients on the free surface (12) become

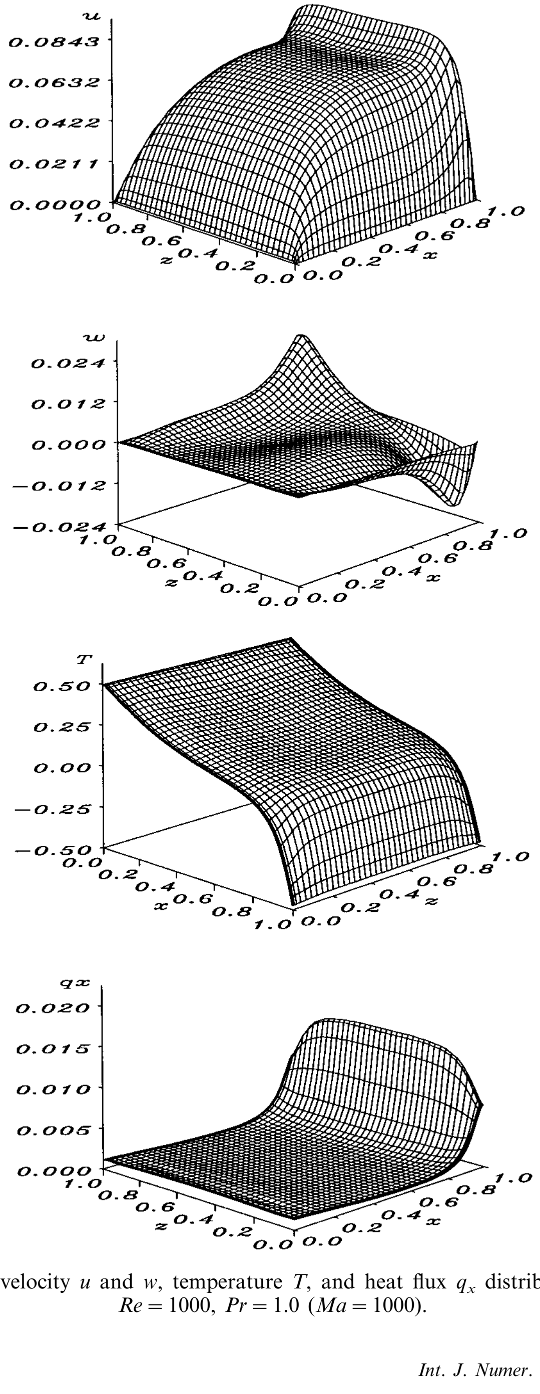

Figure 11. The steady state velocity u and w, temperature T, and heat flux q_x distribution on the free surface for $Re = 1000$, $Pr = 1.0$ ($Ma = 1000$).

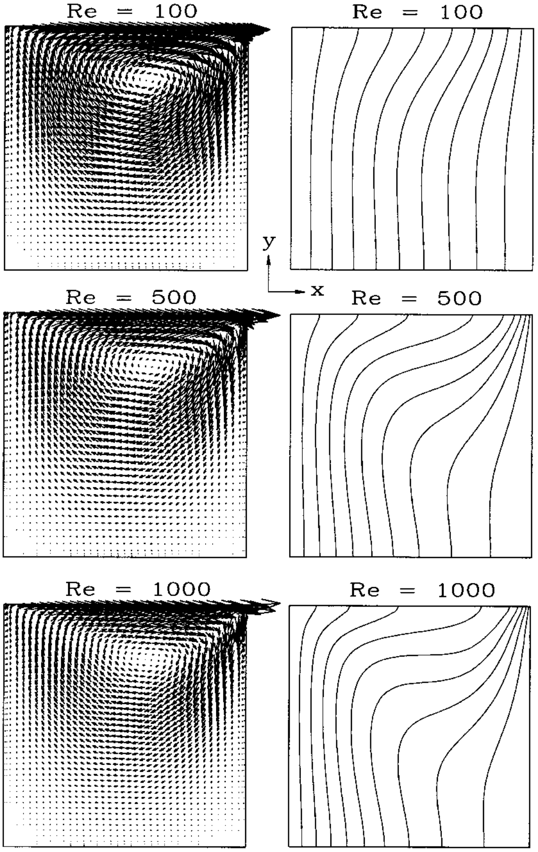

Figure 12. The steady state velocity vectors and temperature contours on the plane of $z = 0.5$ for $Pr = 1.0$.

$$q_z = 0, \quad \text{on } z = 0, 1, \tag{25}$$

$$q_y = 0, \quad \text{on } y = 0, 1, \tag{26}$$

$$\left.\begin{aligned} \omega_z &= -Ma\, q_x \\ \omega_x &= Ma\, q_z \end{aligned}\right\} \quad \text{on } y = 1. \tag{27}$$

Equation (27) describes the boundary conditions on the free surface in the context of the first-order system of equations used in the LSFEM. It is worth mentioning that, although two additional variables, vorticity $\boldsymbol{\omega}$ and heat flux $\mathbf{q}$, are included in the first-order system of equations, no artificial boundary conditions for vorticity and heat flux are necessary at the boundary where velocity and temperature boundary conditions are specified.

3. NUMERICAL METHOD

A time-accurate algorithm has been developed for three-dimensional incompressible flow and natural convection [15]. In this work, the algorithm is used to solve two- and three-dimensional thermocapillary flows. The algorithm is based on an implicit, fully coupled and time-accurate solution in terms of primitive variables of first-order velocity–pressure–vorticity–temperature–heat flux formulation of the Navier–Stokes equations and energy balance equation. Temporal discretization of Equations (17) and (20) is implemented by the Crank–Nicolson method with second-order accuracy in time,

$$\frac{\mathbf{u}^{(n+1)}}{\Delta\tilde{t}} + \left[\mathbf{u}\cdot\nabla\mathbf{u} + \nabla p + \frac{1}{Re}\nabla\times\boldsymbol{\omega} - \frac{Bo}{Re}T\frac{\mathbf{g}}{|\mathbf{g}|}\right]^{(n+1)} = \mathbf{f}_{\mathbf{u}}^{(n)}, \tag{28}$$

$$\nabla\cdot\mathbf{u}^{(n+1)} = 0, \tag{29}$$

$$\boldsymbol{\omega}^{(n+1)} - \nabla\times\mathbf{u}^{(n+1)} = 0, \tag{30}$$

$$\nabla\cdot\boldsymbol{\omega}^{(n+1)} = 0, \tag{31}$$

$$\frac{T^{(n+1)}}{\Delta\tilde{t}} + (\mathbf{u}\cdot\nabla T)^{(n+1)} + \nabla\cdot\mathbf{q}^{(n+1)} = f_T^{(n)}, \tag{32}$$

$$\mathbf{q}^{(n+1)} + \frac{1}{Pe}\nabla T^{(n+1)} = 0, \tag{33}$$

$$\nabla\times\mathbf{q}^{(n+1)} = 0, \tag{34}$$

where superscript n denotes the nth time level, and

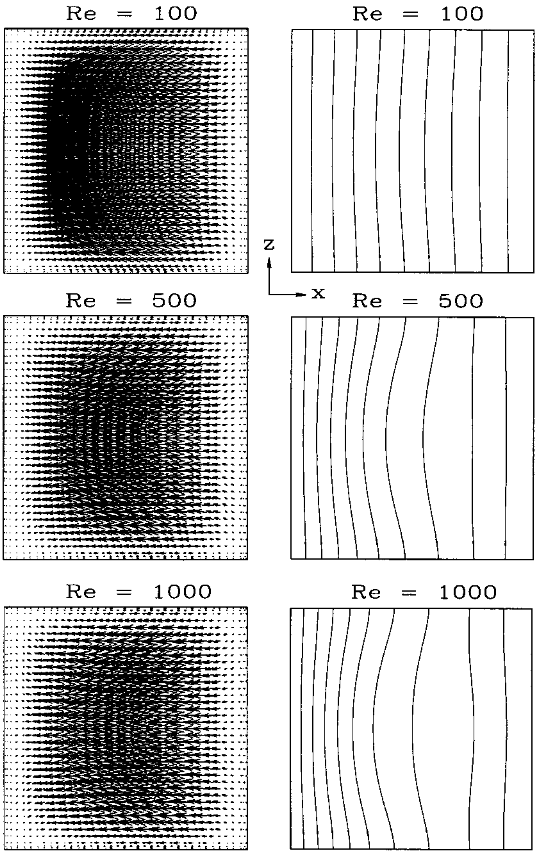

Figure 13. The steady state velocity vectors and temperature contours on the plane of $y = 0.5$ for $Pr = 1.0$.

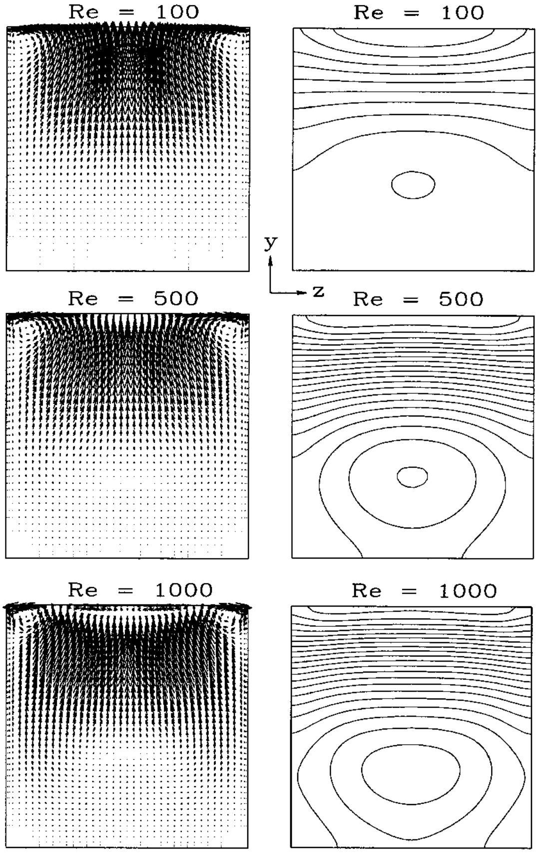

Figure 14. The steady state velocity vectors and temperature contours on the plane of $x = 0.5$ for $Pr = 1.0$.

$$\mathbf{f}_{\mathbf{u}}^{(n)} = \frac{\mathbf{u}^{(n)}}{\Delta\tilde{t}} - \left[\mathbf{u}\cdot\nabla\mathbf{u} + \nabla p + \frac{1}{Re}\nabla\times\boldsymbol{\omega} - \frac{Bo}{Re}T\frac{\mathbf{g}}{|\mathbf{g}|}\right]^{(n)}, \tag{35}$$

$$f_T^{(n)} = \frac{T^{(n)}}{\Delta\tilde{t}} = [\mathbf{u}\cdot\nabla T + \nabla\cdot\mathbf{q}]^{(n)}, \tag{36}$$

where $\Delta\tilde{t} = 1/2\Delta t$ and Δt is the time step.

The convective terms in Equations (28) and (32) are linearized by Newton's method with extensive linearization steps,

$$(\mathbf{u}\cdot\nabla\mathbf{u})^{(n+1)} = \mathbf{u}^{(n+1,m)}\cdot\nabla\mathbf{u}^{(n+1,m+1)} + \mathbf{u}^{(n+1,m+1)}\cdot\nabla\mathbf{u}^{(n+1,m)} - (\mathbf{u}\cdot\nabla\mathbf{u})^{(n+1,m)}, \tag{37}$$

$$(\mathbf{u}\cdot\nabla T)^{(n+1)} = \mathbf{u}^{(n+1,m)}\cdot\nabla T^{(n+1,m+1)} + \mathbf{u}^{(n+1km+1)}\cdot\nabla T^{(n+1,m)} - (\mathbf{u}\cdot\nabla T)^{(n+1,m)}. \tag{38}$$

Substituting Equations (37) and (38) into the equation system (28)–(34), one gets,

$$\frac{\mathbf{u}^{(n+1,m+1)}}{\Delta\tilde{t}} + \mathbf{u}^{(n+1,m)}\cdot\nabla\mathbf{u}^{(n+1,m+1)} + \mathbf{u}^{(n+1,m+1)}\cdot\nabla\mathbf{u}^{(n+1,m)}$$

$$+\left(\nabla p + \frac{1}{Re}\nabla\times\boldsymbol{\omega} - \frac{Bo}{Re}T\frac{\mathbf{g}}{|\mathbf{g}|}\right)^{(n+1,m+1)} = \mathbf{f}_{\mathbf{u}}^{(n)} + \mathbf{g}_{\mathbf{u}}^{(n+1,m)}, \tag{39}$$

$$\nabla\cdot\mathbf{u}^{(n+1,m+1)} = 0, \tag{40}$$

$$\omega^{(n+1,m+1)} - \nabla \times \mathbf{u}^{(n+1,m+1)} = 0, \tag{41}$$

$$\nabla \cdot \omega^{(n+1,m+1)} = 0, \tag{42}$$

$$\frac{T^{(n+1,m+1)}}{\Delta \tilde{t}} + \mathbf{u}^{(n+1,m)} \cdot \nabla T^{(n+1,m+1)} + \mathbf{u}^{(n+1,m+1)} \cdot \nabla T^{(n+1,m)} + \nabla \cdot \mathbf{q}^{(n+1,m+1)}$$

$$= f_T^{(m)} + g_T^{(n+1,m)}, \tag{43}$$

$$\mathbf{q}^{(n+1,m+1)} + \frac{1}{Pe} \nabla T^{(n+1,m+1)} = 0, \tag{44}$$

$$\nabla \times \mathbf{q}^{(n+1,m+1)} = 0, \tag{45}$$

where

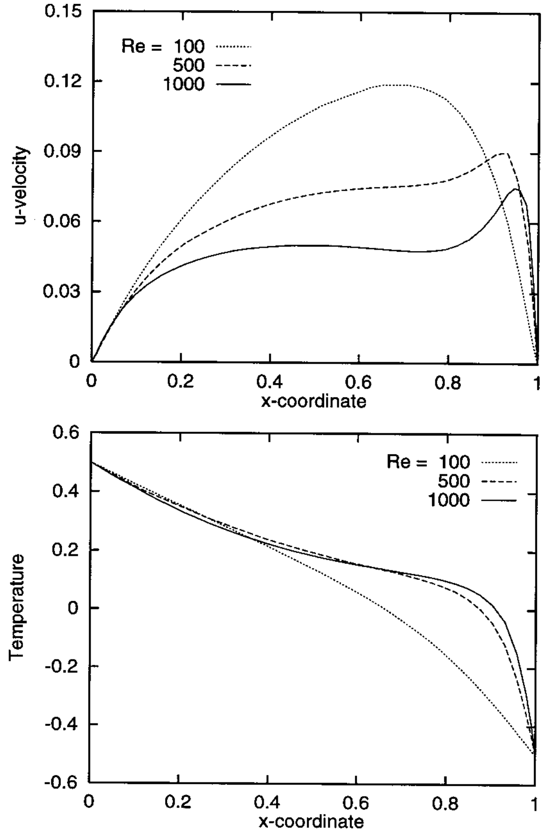

Figure 15. The steady state distributions of velocity u and temperature T along $z = 0.5$ on the free surface for $Pr = 1.0$.

Table I. Computer memory and CPU times on a HP-735 workstation

Number of elements	Storage (Mb)	Average CPU times for a Newton iteration (s)
$30 \times 30 \times 30$	45	38
$40 \times 40 \times 40$	104	98
$50 \times 50 \times 50$	201	287

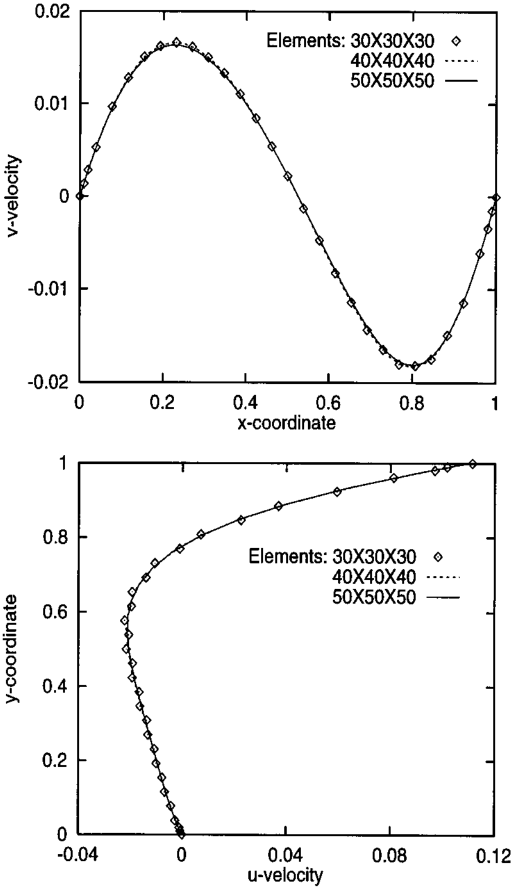

Figure 16. Mesh refinement calculations for velocity u and v along the center lines for $Re = 100$ and $Pr = 1.0$.

$$\left.\begin{aligned} \mathbf{g}_{\mathbf{u}}^{(n+1,m)} &= (\mathbf{u}\cdot\nabla\mathbf{u})^{(n+1,m)} \\ g_T^{(n+1,m)} &= (\mathbf{u}\cdot\nabla T)^{(n+1,m)} \end{aligned}\right\}, \tag{46}$$

and superscript m denotes the mth Newton iteration step. Extensive linearization steps will be used in the algorithm to achieve a high accurate solution.

As mentioned before, the boundary conditions (27), i.e. both components ω_z, ω_x and heat flux components q_x, q_z are unknown on the free surface. In the following, two simple ways are proposed to treat the boundary conditions on the free surface (Equation (27)) in an iterative manner:

(1) using vorticity components ω_z and ω_x as the boundary conditions that are calculated by heat flux components q_x and q_z at the previous Newton linearization step,

$$\left.\begin{aligned} \omega_z^{(n+1,m)} &= -\,Ma\, q_x^{(n+1,m)} \\ \omega_x^{(n+1,m)} &= Ma\, q_z^{(n+1,m)} \end{aligned}\right\} \quad \text{on } y = 1; \tag{47}$$

(2) using heat flux components q_x and q_z as the boundary conditions that are calculated by vorticity components ω_z, ω_x at the previous Newton linearization step,

$$\left.\begin{aligned} q_x^{(n+1,m)} &= -\frac{\omega_z^{(n+1,m)}}{Ma} \\ q_y^{(n+1,m)} &= \frac{\omega_x^{(n+1,m)}}{Ma} \end{aligned}\right\} \quad \text{on } y=1. \tag{48}$$

Numerical experiment shows that for the boundary conditions (47), if q_x and q_y are oscillating, the oscillations will be amplified by Ma times and the oscillating vorticity boundary conditions will cause all the results to oscillate. Since heat flux components q_z and q_y are specified on the vertical walls ($y, z = 0, 1$) and Constraint 5 sets a kinematic relationship between heat flux components so as to eliminate the oscillations of the components, an accurate solution of heat flux can be obtained on the free surface. Therefore, it is very important for thermocapillary problems to use Constraint 5 to obtain accurate solutions. For boundary conditions (48), however, because no vorticity components are specified on the boundaries, vorticity components are not restricted with fixed boundary values. Small perturbations of vorticity components may cause a large error, even if the vorticity components still satisfy Constraint 4. Accurate vorticity approximations cannot be always obtained by the boundary conditions (48) because the numerical solutions do not guarantee convergence. Therefore, the boundary conditions (47) for the thermocapillary flow problem are recommended.

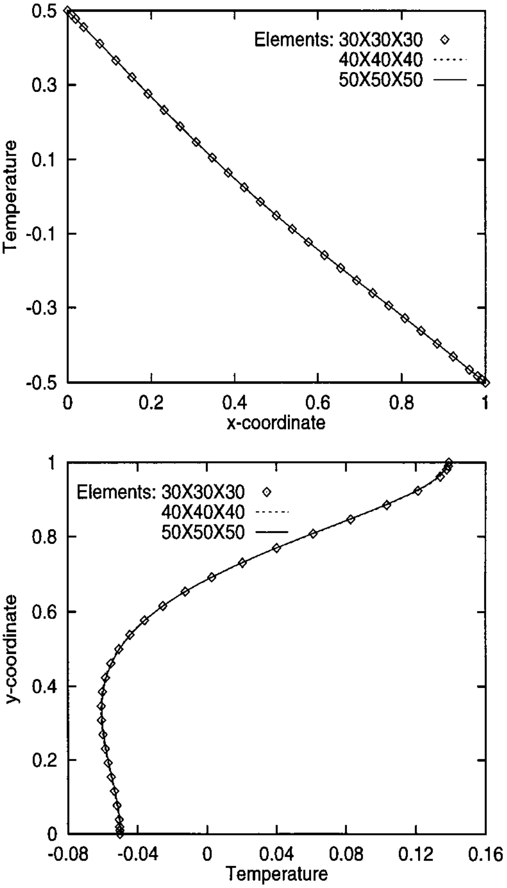

Figure 17. Mesh refinement calculations for temperature along the center lines for $Re = 100$ and $Pr = 1.0$.

The structure of the algorithm for the accurate transient solution is shown in Figure 2, which consists of three iterative loops: (1) time loop—to advance the solution by using the result of the previous time level until the termination time is reached or a steady state solution is obtained, (2) Newton's linearization iteration—to specify the vorticity components ω_x and ω_z as boundary conditions on the free surface for each mth Newton's linearization level and to linearize the non-linear convective terms by extensive iteration steps at the $(n+1)$th time level; and (3) Jacobi conjugate gradient iteration—to solve a SPD linear system of equations at the $(n+1)$th time level and the $(m+1)$th linearization step until the residuals of the linear system are sufficiently small.

The initial boundary value problem (4)–(9), (39)–(45), (24)–(26) and (47) can simply be expressed as

$$\{\mathscr{L}\{\mathrm{v}\}\}^{(n+1,m+1)} = \{\mathbf{f}\}^{(n)} + \{\mathbf{g}\}^{(n+1,m)} \quad \text{in } \Omega, \quad t > 0, \tag{49}$$

$$[\mathscr{B}]\cdot\{\mathbf{v}(\mathbf{x},t)\} = \{\mathbf{g}_d(\mathbf{x},t)\} \quad \text{on } \Gamma_{\mathrm{D}}, \quad t \geq 0, \tag{50}$$

$$\{\mathbf{v}(\mathbf{x},0)\} = \{\mathbf{v}_0(\mathbf{x})\} \quad \text{in } \Omega, \quad t = 0, \tag{51}$$

where $\{\mathbf{v}\} = \{u, v, w, p, \omega_x, \omega_y, \omega_z, T, q_x, q_y, q_z\}^T$, $[\mathscr{B}]$ is the coefficient matrix of boundary conditions, $\{\mathbf{g}_d(\mathbf{x},t)\}$ and $\{\mathbf{v}_0(\mathbf{x})\}$ are the given functions of boundary and initial conditions; and the operator matrix can be denoted in the form of block matrix as

$$\mathscr{L} = \begin{pmatrix} \mathscr{L}_{11} & \mathscr{L}_{12} \\ \mathscr{L}_{21} & \mathscr{L}_{22} \end{pmatrix}^{(n+1,m)}, \tag{52}$$

where the submatrices are

$$\mathscr{L}_{11} = \left[\begin{array}{ccccccc} d^{(u)} & \dfrac{\partial u}{\partial y} & \dfrac{\partial u}{\partial z} & \dfrac{\partial}{\partial x} & 0 & \dfrac{-1}{Re}\dfrac{\partial}{\partial z} & \dfrac{1}{Re}\dfrac{\partial}{\partial y} \\ \dfrac{\partial v}{\partial x} & d^{(v)} & \dfrac{\partial v}{\partial z} & \dfrac{\partial}{\partial y} & \dfrac{1}{Re}\dfrac{\partial}{\partial z} & 0 & \dfrac{-1}{Re}\dfrac{\partial}{\partial x} \\ \dfrac{\partial w}{\partial x} & \dfrac{\partial w}{\partial y} & d^{(w)} & \dfrac{\partial}{\partial z} & \dfrac{-1}{Re}\dfrac{\partial}{\partial y} & \dfrac{1}{Re}\dfrac{\partial}{\partial x} & 0 \\ \dfrac{\partial}{\partial x} & \dfrac{\partial}{\partial y} & \dfrac{\partial}{\partial z} & 0 & 0 & 0 & 0 \\ 0 & \dfrac{\partial}{\partial z} & -\dfrac{\partial}{\partial y} & 0 & 1 & 0 & 0 \\ -\dfrac{\partial}{\partial z} & 0 & \dfrac{\partial}{\partial x} & 0 & 0 & 1 & 0 \\ \dfrac{\partial}{\partial y} & -\dfrac{\partial}{\partial x} & 0 & 0 & 0 & 0 & 1 \\ 0 & 0 & 0 & 0 & \dfrac{\partial}{\partial x} & \dfrac{\partial}{\partial y} & \dfrac{\partial}{\partial z} \end{array} \right], \tag{53}$$

$$\mathscr{L}_{12}=\begin{pmatrix} 0 & 0 & 0 & 0 \\ -\dfrac{Bo}{Re} & 0 & 0 & 0 \\ 0 & 0 & 0 & 0 \\ \dots & \dots & \dots & \dots \\ 0 & 0 & 0 & 0 \end{pmatrix}, \tag{54}$$

$$\mathscr{L}_{21}=\begin{pmatrix} \dfrac{\partial T}{\partial x} & \dfrac{\partial T}{\partial y} & \dfrac{\partial T}{\partial z} & 0 & \dots & 0 \\ 0 & \dots & \dots & \dots & \dots & 0 \\ \dots & \dots & \dots & \dots & \dots & \dots \\ 0 & \dots & \dots & \dots & \dots & 0 \end{pmatrix}, \tag{55}$$

$$\mathscr{L}_{22}=\begin{pmatrix} d & \dfrac{\partial}{\partial x} & \dfrac{\partial}{\partial y} & \dfrac{\partial}{\partial z} \\ \dfrac{1}{Ma}\dfrac{\partial}{\partial x} & 1 & 0 & 0 \\ \dfrac{1}{Ma}\dfrac{\partial}{\partial y} & 0 & 1 & 0 \\ \dfrac{1}{Ma}\dfrac{\partial}{\partial z} & 0 & 0 & 1 \\ 0 & 0 & -\dfrac{\partial}{\partial z} & \dfrac{\partial}{\partial y} \\ 0 & \dfrac{\partial}{\partial z} & 0 & -\dfrac{\partial}{\partial x} \\ 0 & -\dfrac{\partial}{\partial y} & \dfrac{\partial}{\partial x} & 0 \end{pmatrix}, \tag{56}$$

and the coefficients are defined as

$$d=u\frac{\partial}{\partial x}+v\frac{\partial}{\partial y}+w\frac{\partial}{\partial z}+\frac{1}{\Delta t}, \tag{57}$$

$$d^{(u)}=d+\frac{\partial u}{\partial x}, \tag{58}$$

$$d^{(v)}=d+\frac{\partial v}{\partial y}, \tag{59}$$

$$d^{(w)}=d+\frac{\partial w}{\partial z}, \tag{60}$$

and the right-hand side vectors are

$$\{\mathbf{g}\}^{(n)} = \left\{ \begin{array}{c} \dfrac{u}{\Delta t} - \tilde{\theta}\left[\mathbf{u}\cdot\nabla u + \dfrac{\partial p}{\partial x} + \dfrac{1}{Re}\left(\dfrac{\partial \omega_z}{\partial y} - \dfrac{\partial \omega_y}{\partial z}\right)\right] \\ \dfrac{v}{\Delta t} - \tilde{\theta}\left[\mathbf{u}\cdot\nabla v + \dfrac{\partial p}{\partial y} + \dfrac{1}{Re}\left(\dfrac{\partial \omega_x}{\partial z} - \dfrac{\partial \omega_x}{\partial y}\right) - \dfrac{Bo}{Re}\,T\right] \\ \dfrac{w}{\Delta t} - \tilde{\theta}\left[\mathbf{u}\cdot\nabla w + \dfrac{\partial p}{\partial z} + \dfrac{1}{Re}\left(\dfrac{\partial \omega_y}{\partial x} - \dfrac{\partial \omega_x}{\partial y}\right)\right] \\ 0 \\ \vdots \\ 0 \\ \dfrac{T}{\Delta t} - \tilde{\theta}(\mathbf{u}\cdot\nabla T + \nabla\cdot\mathbf{q}) \\ 0 \\ \vdots \\ 0 \end{array} \right\}^{(n)}, \tag{61}$$

$$\{\mathbf{f}\}^{(n+1,m)} = \left\{ \begin{array}{c} \mathbf{u}\cdot\nabla u \\ \mathbf{u}\cdot\nabla v \\ \mathbf{u}\cdot\nabla w \\ 0 \\ \vdots \\ 0 \\ \mathbf{u}\cdot\nabla T \\ 0 \\ \vdots \\ 0 \end{array} \right\}^{(n+1,m)}. \tag{62}$$

4. NUMERICAL RESULTS AND DISCUSSION

4.1. Two-dimensional thermocapillary flows

The first two case studies are two-dimensional augmenting and opposing buoyant thermocapillary flows in a square cavity. The side wall at the left-hand side is maintained at a higher temperature than the side wall at the right-hand side. The bottom wall and the top free surface are insulated. A mesh system of 100 × 100 bilinear elements are used to achieve high resolution results. The parameters are set as $Ma = 8.3 \times 10^3$, $Pr = 0.0149$ and $Gr = 3.09 \times 10^6$.

Augmenting flow is a flow driven by the buoyancy force due to temperature gradients acting in the same direction as the surface tension force on the free surface. Figure 3 shows the clockwise augmenting flow in a square cavity. The primary flow vortex is seen to exist near the right wall, and the velocity vectors suggest the formation of a boundary layer near the top right wall. The temperature contours show the distortion of the conduction profiles by the thermocapillary flow, and the streamfunctions demonstrate the existence of a strong vortex. For this case study, no literature result is available for comparison.

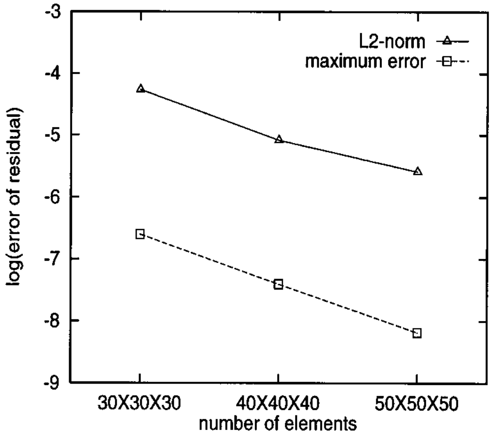

(a)

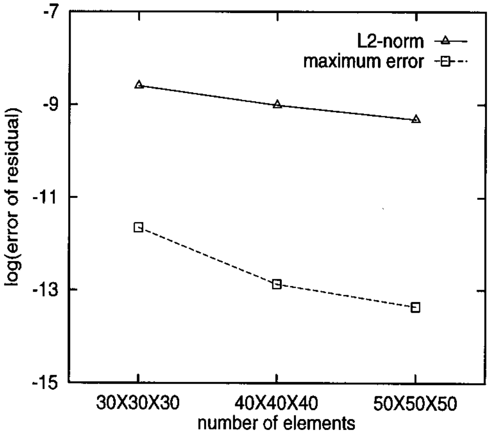

(b)

Figure 18. Error analysis of residuals for (a) the solenoidality of vorticity and (b) the non-rotationality of heat flux.

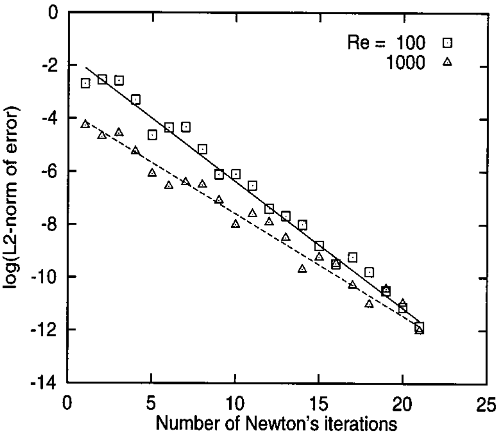

Figure 19. Convergence history of Newton's method for 3D thermocapillary flows.

For opposing buoyant thermocapillary flows, the surface tension-driven flow opposes the buoyancy-driven flow. The variation of surface tension with temperature is negative. Figure 4 shows that the buoyancy-induced vortex is confined to the middle of the cavity, but a strong counterrotating vortex-driven by the surface tension force is found at the upper left corner of the cavity. The results compare well with those given by Shyy and Chen [23].

In the third case study, the intention is to simulate the oscillatory thermocapillary flow of a low Prandtl number fluid in a rectangular cavity with aspect ratio of 4. The dimensionless parameters are set as $Re = 67$, $Pr = 0.0149$ and $Gr = 2.0 \times 10^4$. Mundrane and Zebib [5] showed the existence of a periodic flow solution for these parameters. Figure 5 shows the streamfunctions, temperature contours, vorticity and velocity vectors for the flow system in the periodic state at a dimensionless time level of 45. Figure 6 shows the time history of the dimensionless temperature at the center of the cavity. Although it is not possible to have exact comparison between the transient results here and those by Mundrane and Zebib [5], Figures 5 and 6 are qualitatively the same as theirs.

4.2. Three-dimensional thermocapillary flows

Now, consider three-dimensional thermocapillary flows under a low gravity condition, i.e. $Bo = 0$. The following case studies are relevant to crystal growth processes in a low gravity condition, at which buoyancy-induced flows (natural convection) become negligible compared with dominant thermocapillary flows.

4.2.1. Temporal features. To study the temporal features of three-dimensional thermocapillary flows, velocity vectors and temperature contours on the cross-section ($x, y, z = 0.5$) of the cavity at different time levels are shown in Figures 7–9. The velocity vectors, on the cross-section of $z = 0.5$ for the thermocapillary flow, as shown in Figure 7, are similar to those for low Reynolds number lid-driven cavity flow. However, as shown in Figure 8, the velocity vector on the cross-section of $y = 0.5$ are totally different from those for lid-driven cavity flows [14]. The temperature contours become more tortuous with time, as shown in Figures 7 and 8. On the cross-section of $x = 0.5$, two vortices are observed at the corners of the free surface and temperature contours move down with time, as shown in Figure 9. The velocity component u and the temperature profile along the center line ($z = 0.5$) on the free surface at different time levels for $Re = 1000$ and $Pr = 1.0$ are given in Figure 10. The peak of the velocity component u moves toward the vertical wall of $x = 1.0$ with time. Near the vertical wall of $x = 1.0$, the velocity profile of component u becomes steep as the temperature increases with time. The steady state velocity u and w, temperature T, and heat flux q_x distributions on the free surface are shown in Figure 11.

4.2.2. Effects of Reynolds number. Consider flow patterns for Reynolds numbers of $Re = 100$–1000, with a fixed Prandtl number of $Pr = 1.0$. Steady state velocity vectors and temperature contours on the center cross-section ($x, y, z = 0.5$) of the cavity for different Reynolds numbers are shown in Figures 12–14. No significant difference of velocity vectors is observed, but the distortion of temperature contours becomes more pronounced with the increase of Reynolds numbers on the cross-sections of $z, y = 0.5$, as shown in Figures 12 and 13. On the cross-sections of $x = 0.5$, the vortices at the corners of the free surface become stronger, and temperature contours move down with the increase of Reynolds number, as shown in Figure 14. The steady state velocity component u and the temperature profile along the center line of $z = 0.5$ on the free surface for different Reynolds numbers and $Pr = 1.0$ are given in Figure 15. The peak of the velocity component u decreases with the increase of Reynolds number, and the velocity profile becomes steeper at the wall. But the temperature increases near the vertical wall of $x = 1.0$ with the increase in Reynolds number.

It should be mentioned that the vortices at the corners of the free surface for $Re = 100$ and $Pr = 1.0$ are not observed in the work by Babu and Korpela [8]. Thus, the following mesh refinement study was carried out to verify the LSFEM result by using three mesh systems of $30 \times 30 \times 30$, $40 \times 40 \times 40$ and $50 \times 50 \times 50$. A uniform grid is used throughout the domain, with two fine grids along the walls. The average CPU times for a Newton iteration and computer memory requirements are given in Table I. The results for velocity components u and v, and temperature T along the center lines of x, $z = 0.5$ and y, $z = 0.5$ for $Re = 100$ and $Pr = 1.0$ are shown in Figures 16 and 17. Figure 16 shows that there are slight oscillations of velocity components for a mesh system of $30 \times 30 \times 30$. The temperature profiles for all the mesh systems are consistent with each other, as shown in Figure 17. The residuals of Equations (22) and (23) are defined for three-dimensional flows as

$$R_{\omega} = \nabla \cdot \boldsymbol{\omega}, \tag{63}$$

and

$$R_{\mathbf{q}} = \sqrt{\left(\frac{\partial q_z}{\partial y} - \frac{\partial q_y}{\partial z}\right)^2 + \left(\frac{\partial q_x}{\partial z} - \frac{\partial q_z}{\partial x}\right)^2 + \left(\frac{\partial q_y}{\partial x} - \frac{\partial q_x}{\partial y}\right)^2}. \tag{64}$$

In this study, particular interest was taken in the residuals R_{ω} and R_{q} because these residuals reveal how well Constraints 4 and 5 (Equations (22) and (23)) are reinforced in the LSFEM. The l2-norm and maximum absolute value of the residuals defined in Equations (63) and (64) for different mesh systems at the steady state are shown in Figure 18, for $Re = 100$ and $Pr = 1.0$ ($Ma = 100$). The convergence history of the Newton method for three-dimensional thermocapillary flows at steady state is given in Figure 19 for different Reynolds numbers and $Pr = 1$. The result at $t = 30$ is used as the initial guess to calculate the steady state solutions. At this time level, the velocity components are still quite different from the steady state values. It takes about 20 Newton steps and 5800 Jacobi conjugate gradient (JCG) iterations to reach the steady state. It is worth mentioning that it takes about 4200 JCG iterations for the first Newton step. From Figure 19, it is obvious that the l2-norm decreases with the increase of Reynolds number in a manner consistent with the result of two-dimensional, lid-driven cavity flow obtained by Jiang [24]. This implies that it takes more Newton linearization steps for convergence for higher Reynolds number flows.

5. CONCLUSIONS

A LSFEM with a matrix-free Jacobi conjugate gradient algorithm and Newton's linearization is used to simulate a variety of 2D and 3D transient thermocapillary flows. Numerical results for 2D augmenting, opposing, and oscillatory flows compare well with the literature. Transient and steady state solutions are presented for 3D flows for Prandtl number $Pr = 1.0$ and Reynolds number in the range $Re = 100-1000$. The mesh refinement study is carried out to validate the 3D numerical results. This work demonstrates that the iterative procedure, i.e. Equation (47), is a robust approach to treat the capillary-traction boundary conditions for thermocapillary flows.

ACKNOWLEDGMENTS

The work was partially supported by the National Science Foundation (NSF/KY EPSCoR program), the Center for Computational Sciences at the University of Kentucky and the US Environmental Protection Agency.

REFERENCES

1. A. Zebib, G. Homsy and E. Meiburg, 'High Marangoni number convection in a square cavity', *Phys. Fluids*, **28**, 3467–3476 (1985).
2. B.M. Carpenter and G.M. Homsy, 'High Marangoni number convection in a square cavity: Part II', *Phys. Fluids*, **2**, 137–149 (1990).
3. W. Shyy and M.H. Chen, 'A study of the transport process of buoyance-induced and thermocapillary flow of molten alloy', *Comput. Methods Appl. Mech. Eng.*, **103**, 333–358 (1993).
4. H.B. Hadid and B. Roux, 'Buoyancy- and thermocapillary-driven flows in differentially heated cavities for low Prandtl number fluids', *J. Fluid Mech.*, **235**, 1–36 (1992).
5. M. Mundrane and A. Zebib, 'Oscillatory buoyant thermocapillary flow', *Phys. Fluids*, **6**, 3294–3305 (1994).
6. M. Kanouff and R. Greif, 'Oscillations in a thermocapillary square cavity', *Int. J. Heat Mass Transf.*, **37**, 885–892 (1994).
7. M. Mundrane and A. Zebib, 'Two- and three-dimensional buoyant thermocapillary convection', *Phys. Fluids*, **5**, 810–818 (1993).
8. V. Babu and S.A. Korpela, 'Three-dimensional thermocapillary convection in a cavity', *Comput. Fluids*, **18**, 229–238 (1990).
9. P.B. Bochev and M.D. Gunzburger, 'Accuracy of least-squares methods for the Navier–Stokes equations', *Comput. Fluids*, **22**, 549–563 (1993).
10. B.N. Jiang, T.L. Lin and L.A. Povinelli, 'Large-scale computation of incompressible viscous flow by least-squares finite element method', *Comput. Methods Appl. Mech. Eng.*, **114**, 213–231 (1994).
11. B.N. Jiang and L.A. Povinelli, 'Least-squares finite element method for fluid dynamics', *Comput. Methods Appl. Mech. Eng.*, **81**, 13–37 (1990).
12. L.Q. Tang, T.W. Cheng and T.T.H. Tsang, 'Transient solutions for three-dimensional lid-driven cavity flows by a least-squares finite element method', *Int. J. Numer. Methods Fluids*, **21**, 413–432 (1995).
13. L.Q. Tang and T.T.H. Tsang, 'A least-squares finite element method for time-dependent incompressible flows with thermal convection', *Int. J. Numer. Methods Fluids*, **17**, 271–289 (1993).
14. L.Q. Tang and T.T.H. Tsang, 'An efficient least-squares finite element method for incompressible flows and transport processes', *Int. J. Comput. Fluid Dyn.*, **4**, 21–39 (1995).
15. L.Q. Tang and T.T.H. Tsang, 'Temporal, spatial and thermal features of 3D Rayleigh–Benard convection by a least-squares finite element method', *Comput. Methods Appl. Mech. Eng.*, **140**, 201–219 (1997).
16. P.B. Bochev and M.D. Gunzburger, 'Analysis of least-squares finite element methods for the Stokes equations', *Math. Comput.*, **63**, 479–506 (1994).
17. P.B. Bochev and M.D. Gunzburger, 'Least-squares methods for the velocity–pressure stress formulation of the Stokes equations', *Comput. Methods Appl. Mech. Eng.*, **126**, 267–287 (1995).
18. Z. Cai, R.D. Lazarov, T. Manteuffel and S. McCormick, 'First-order system least-squares for second-order partial differential equations: Part I', *SIAM J. Numer. Anal.*, **31**, 1785–1799 (1994).
19. A.I. Pehlivanor, G.F. Carey and R.D. Lazarov, 'Least-squares mixed finite elements for second-order elliptic problems', *SIAM J. Numer. Anal.*, **31**, 1368–1377 (1994).
20. P.M. Gresho, 'Incompressible fluid dynamics: some fundamental formulation issue', *Annu. Rev. Fluid Mech.*, **23**, 413–453 (1991).
21. P.M. Gresho, 'Some current CFD issues relative to the incompressible Navier–Stokes equations', *Comput. Methods Appl. Mech. Eng.*, **87**, 201–252 (1991).
22. L.Q. Tang, 'A least-squares finite element method for time-dependent fluid flows and transport phenomena', *Ph.D. Thesis*, University of Kentucky, KY, 1994.
23. W. Shyy and M.H. Chen, 'Interaction of thermocapillary and natural convection flows during solidification: normal and reduced gravity conditions', *J. Crystal Growth*, **108**, 247–261 (1991).
24. B.N. Jiang, 'A least-squares finite element method for incompressible Navier–Stokes problems', *Int. J. Numer. Methods Fluids*, **14**, 843–859 (1992).